

Article

Impact of Sulfur Infiltration Time and Its Content in an N-doped Mesoporous Carbon for Application in Li-S Batteries

Jennifer Laverde ¹, Nataly C. Rosero-Navarro ^{2,*}, Akira Miura ², Robison Buitrago-Sierra ³, Kiyoharu Tadanaga ² and Diana López ¹

¹ Instituto de Química, Facultad de Ciencias Exactas y Naturales, Universidad de Antioquia, Calle 70 No. 52-21, Medellín 050010, Colombia; jennifer.laverde@udea.edu.co (J.L.); diana.lopez@udea.edu.co (D.L.)

² Faculty of Engineering, Hokkaido University, Sapporo 060-8628, Japan; amiura@eng.hokudai.ac.jp (A.M.); tadanaga@eng.hokudai.ac.jp (K.T.)

³ Facultad de Ingeniería, Instituto Tecnológico Metropolitano—ITM, Medellín 050034, Colombia; robinsonbuitrago@itm.edu.co

* Correspondence: rosero@eng.hokudai.ac.jp

Abstract: Li-S batteries are ideal candidates to replace current lithium-ion batteries as next-generation energy storage systems thanks to their high specific capacity and theoretical energy density. Composite electrodes based on carbon microstructures are often used as a host for sulfur. However, sulfur lixiviation, insoluble species formation, and how to maximize the sulfur–carbon contact in looking for improved electrochemical performance are still major challenges. In this study, a nitrogen doped mesoporous carbon is used as a host for sulfur. The S/C composite electrodes are prepared by sulfur melting-diffusion process at 155 °C. The effect of the sulfur melting-diffusion time [sulfur infiltration time] (1–24 h) and sulfur content (10–70%) is investigated by using XRD, SEM, TEM and TGA analyses and correlated with the electrochemical performance in Li-S cells. S/C composite electrode with homogeneous sulfur distribution can be reached with 6 h of sulfur melting-diffusion and 10 wt.% of sulfur content. Li-S cell with this composite shows a high use of sulfur and sufficient electronic conductivity achieving an initial discharge capacity of 983 mA h g⁻¹ and Coulombic efficiency of 99% after 100 cycles.

Keywords: lithium-sulfur battery; lithium-sulfur electrochemical properties; sulfur distribution; pore infiltration; wall thickness changes; mesoporous carbon host



Citation: Laverde, J.; Rosero-Navarro, N.C.; Miura, A.; Buitrago-Sierra, R.; Tadanaga, K.; López, D. Impact of Sulfur Infiltration Time and Its Content in an N-doped Mesoporous Carbon for Application in Li-S Batteries. *Batteries* **2022**, *8*, 58. <https://doi.org/10.3390/batteries8060058>

Academic Editor: Carlos Ziebert

Received: 4 April 2022

Accepted: 13 June 2022

Published: 17 June 2022

Publisher's Note: MDPI stays neutral with regard to jurisdictional claims in published maps and institutional affiliations.



Copyright: © 2022 by the authors. Licensee MDPI, Basel, Switzerland. This article is an open access article distributed under the terms and conditions of the Creative Commons Attribution (CC BY) license (<https://creativecommons.org/licenses/by/4.0/>).

1. Introduction

The development of batteries with high energy density has been a topic of great interest in recent years as they are widely used in numerous applications of daily life [1]. Li-S batteries are promising candidates for the next-generation energy storage devices because of the natural availability, low toxicity, low cost of sulfur, and also the high specific capacity and energy density reaching up to 1675 mA h g⁻¹ and 2600 W h kg⁻¹, respectively compared with conventional Li-ion batteries [2–4]. Despite the high theoretical capacity of the Li-S system, it is not currently at a commercial level. This is mainly due to the easy capacity fade produced by the solubility of the intermediate species of lithium polysulfide ($\text{Li}_2\text{S}_x, 4 \leq x \leq 8$) in the electrolyte (shuttle effect) from initial charge and discharge processes, causing loss of the active material and increase of the electrolyte viscosity [5–7].

The preparation of composite electrodes containing carbonaceous materials with a wide variety of microstructures has been widely studied [8]. The main objective of carbonaceous materials is not only to obtain enough electronic conductivity with the insulating nature of sulfur, but also to strengthen the sulfur retention and prevent the subsequent deactivation of the battery [9]. However, maximizing the sulfur–carbon contact and therefore producing a better electrochemical performance is still a challenge. In this regard,

different synthesis methodologies to enhance the interface contact between sulfur and carbon material have been studied [10,11]. Mechanical milling, gas-phase mixing, and melting-diffusion processes have been used to prepare sulfur/carbon composites; however, the melting-diffusion process can be carried out at lower temperatures (119–159 °C) than those employed in the gas phase by vapor infiltration (~445 °C) [12,13]. These sulfur encapsulation strategies have proven to be efficient to enhance the sulfur-carbon contact, showing results of high specific capacities and stable cycling performance (up to 500 cycles) in the tested batteries. However, the possibility of increasing the sulfur mass load on the electrode to generate the necessary energy density for the current technology requirements is still being investigated [8]. Synthesis parameters such as the sulfur inclusion time, temperature, sulfur content, strongly affect the electrochemical performance of these batteries. The correlation between the synthesis conditions and the electrochemical performance of the Li-S battery is still unclear [14,15].

In this research, we study the preparation of sulfur-carbon (S/C) composite electrodes based on a nitrogen-doped mesoporous carbon (CMK-3) and sulfur infiltration by its melt and diffusion at 155 °C. We focus on two main aspects: the effect of the sulfur infiltration or inclusion into carbonaceous structure understood as the time of sulfur melting-diffusion process (form here sulfur infiltration time) and the sulfur content effect in the composite. Mesoporous carbons have been proposed as promising materials to host sulfur since their high surface area and large pore diameter may allow the inclusion of a larger amount of sulfur within their structure. Particularly, CMK-3 mesoporous carbon has a well-defined interconnected nanostructure with highly ordered porosity obtained by the use of silicon oxide templates such as SBA-15 [16,17]. Furthermore, the structure of CMK-3 can be modified by nitrogen doping through an in-situ nitrogen inclusion methodology. This modification, in addition to promoting the adsorption of sulfur polysulfides, may improve the wettability of electrodes favoring the permeability of the electrolyte inside the material [18]. Figure 1 illustrates the synthesis of 2D mesoporous carbon and their further use as a sulfur host in. The sulfur is expected to fill the pores and to interact with the carbon material while giving enough space to allow contact with liquid electrolyte.

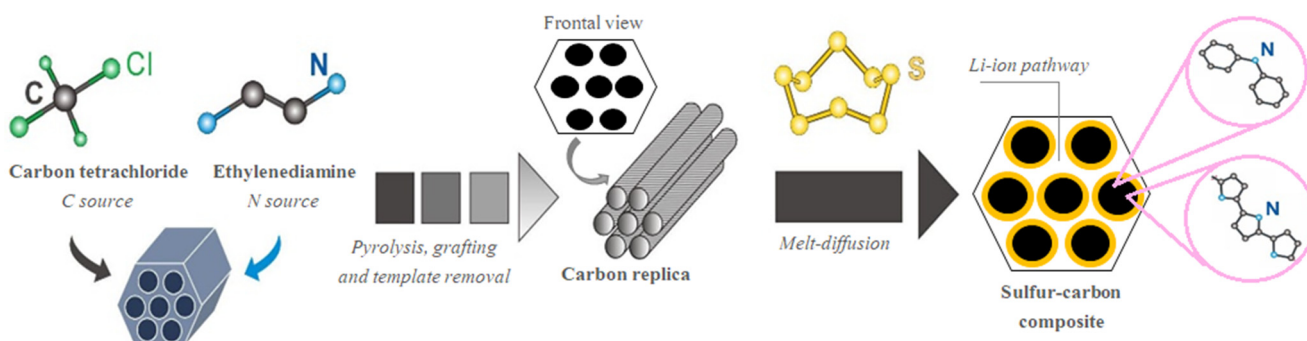


Figure 1. Illustration of the preparation of S/C composite electrodes based on nitrogen-doped mesoporous carbon and sulfur melt-diffusion process.

2. Results and Discussion

2.1. Sulfur Infiltration Time Effect

Nitrogen quantification for the carbonaceous material without sulfur infiltration was carried out using elemental analysis and XPS to determine its total nitrogen content and identify different functionalities generated in the carbonization process given that the pyridinic-N and pyrrolic-N increase the pseudo-capacitance, while the graphitization is due to the graphitic-N and this functionalities have influence in the electrochemical behavior of the studied cells [19,20]. Figure S1 present the high-resolution XPS spectra for N1s. The high-resolution XPS for nitrogen shows a splitting of N1s into four peaks with binding energies of 398.06, 399.13, 400.85, and 402.95 eV corresponding to pyridinic nitrogen, pyrrolic nitrogen, graphitic nitrogen, and oxidized nitrogen respectively. Table 1

present the relevant results focus on nitrogen content and functionalities according to the high-resolution XPS spectra result presented in Figure S1.

Table 1. Elemental composition of the mesoporous carbon by elemental analysis and XPS.

Elemental Analysis				XPS			
C (wt.%)	N (wt.%)	H (wt.%)	O (wt.%)	Nitrogen			
				Graphitic-N	Pyrrolic-N	Pyridinic-N	N-o-
74.6	7.34	1.14	16.9	39.6	10.1	24.3	26

Figure 2 shows physicochemical characterization of the MC and S/C composites at different sulfur infiltration time. Figure 2a displays the nitrogen adsorption/desorption isotherms and pore size distribution for the MC and S/C composites. The MC profile reveals the typical behavior for mesoporous materials with type IV isotherm [21], the hysteresis loop is observed between 0.4–0.8 of relative pressure P/P_0 attributed to capillary condensation of nitrogen inside the pores being indicative of mesopores presence in the carbonaceous structure with cylindrical pores channels [2,3]. The S/C composites reveal a different isotherm behavior which is not necessarily related to a change in the type of porosity or with the collapse of the carbonaceous material structure during the infiltration. The non-infiltrated sulfur could form layer deposits outside the pores that is supposed to be the reason for this profile. The MC achieves a surface area of $872.8 \text{ m}^2 \text{ g}^{-1}$ and pore volume of $1.04 \text{ cm}^3 \text{ g}^{-1}$ by BET analysis. Two types of mesoporous are observed for MC and S/C composites (inset of Figure 2a) with the diameters centered about 37 \AA and 89 \AA . After the infiltration with 70 wt.% of sulfur, a considerable decrease in the pore volume suggests that sulfur is infiltrated in the MC structure [16]. Figure 2b shows the XRD patterns of the S/C composites at different sulfur infiltration times. XRD patterns of elemental sulfur and the MC are included as references. The XRD pattern of elemental sulfur presents sharp-peaks corresponding to crystalline orthorhombic phase with the space group Fddd (ICSD 98-041-2326) [3,22,23]. The XRD pattern of MC shows a mainly amorphous structure with two broad peaks at $2\theta = 30^\circ$ and 51° corresponding to (002) and (011) planes of ordered hexagonal structure respectively (ICSD 98-061-7290) [24,25]. The XRD patterns of the S/C composites correspond with the peaks attributed to the orthorhombic phase of sulfur. The intensity of these peaks seems to decrease with the increase of infiltration time, in which an infiltration time of 6 h shows a visible change of the tendency with a broad background (amorphization) in the region of $2\theta = 25\text{--}35^\circ$, similar to the XRD pattern of the mesoporous carbon. At longer infiltration times of 12 h and 24 h, the peaks corresponding to the orthorhombic phase of sulfur are again observed. The orthorhombic sulfur phase present in the S/C composites is associated with a not fully efficient sulfur infiltration [26–31]. At 6 h, the infiltration of the sulfur into the MC structure (mesopore filling) is evidenced by the broad reflection peak between $26\text{--}35^\circ$ indicating an enhanced dispersion of sulfur; however, the presence of low-intensity peaks of sulfur also suggests that a portion of this still remains un-infiltrated) [32–34].

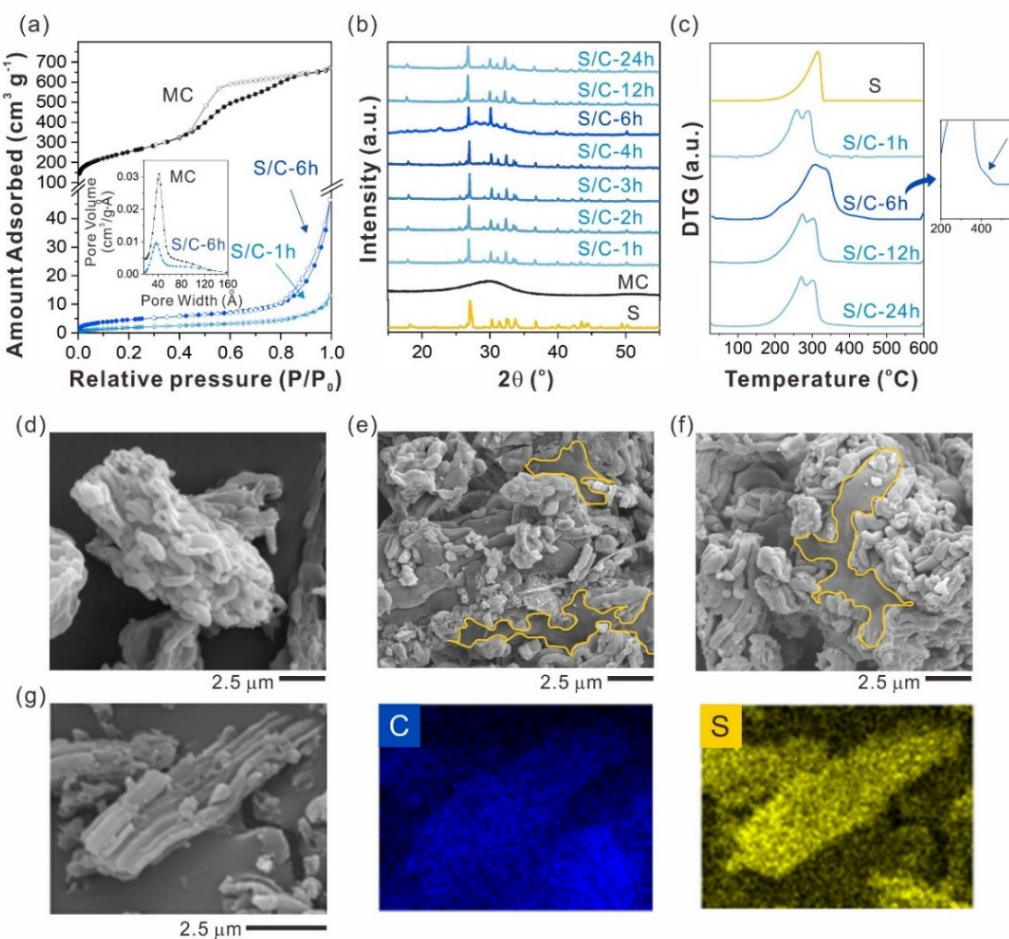


Figure 2. (a) Adsorption and desorption isotherms for mesoporous carbon and S/C composites at 1 and 6 h of infiltration. Unfilled symbols correspond to desorption. Inset corresponds to pore size distribution. (b) XRD patterns of elemental sulfur, mesoporous carbon, and the S/C composites at different infiltration times. (c) DTG curves for sulfur and S/C composites at different time infiltrations. SEM analysis of (d) mesoporous carbon, and the S/C composites: (e) S/C-1 h, (f) S/C-24 h and, (g) S/C-6 h. Yellow lines in (e,f) denote the sulfur deposition. EDX mapping including carbon and sulfur in included for S/C-6 h composite.

Figure 2c shows the differential thermogravimetric analysis curves (dW/dT , DTG) of sulfur and S/C composites at different sulfur infiltration times. Figure S2 shows thermogravimetric analyses (TGA) used to obtain Figure 2c. The sulfur and S/C composites show a clear weight loss approximately between $200\text{ }^{\circ}\text{C}$ and $450\text{ }^{\circ}\text{C}$ (Figure S2) corresponding to the sulfur melting and sublimation processes [35,36]. The sulfur content, considering this weight loss, resulted in ca. 69 wt.% which confirms a negligible loss of sulfur during the melting-diffusion process. The DTG curve of sulfur shows a single peak at $300\text{ }^{\circ}\text{C}$ corresponding to its melting-sublimation process. However, DTG profiles of S/C composites show a broad multi-peak revealing that the sulfur weight loss takes place in more than one sublimation event [15]. DTG profile of S/C-1 h shows two main sulfur weight losses at $256\text{ }^{\circ}\text{C}$ and $289\text{ }^{\circ}\text{C}$. DTG profile of S/C-6 h shows four main sulfur weight losses at $238\text{ }^{\circ}\text{C}$, $308\text{ }^{\circ}\text{C}$, $336\text{ }^{\circ}\text{C}$ and $421\text{ }^{\circ}\text{C}$ (zooming inset of Figure 2c). DTG profile of S/C-12 h and S/C-24 h shows three main sulfur weight losses at $274\text{ }^{\circ}\text{C}$, $302\text{ }^{\circ}\text{C}$, and $379\text{ }^{\circ}\text{C}$ and, $271\text{ }^{\circ}\text{C}$, $301\text{ }^{\circ}\text{C}$, and $382\text{ }^{\circ}\text{C}$, respectively.

According to K. Suzuki et al. and Z. Li et al. [15,37], there is a close interaction between sulfur and carbon material when the sulfur sublimation temperature is higher than $280\text{ }^{\circ}\text{C}$, a weight loss above this temperature is associated with sulfur inside the pore of the carbonaceous material, the sulfur sublimed at lower temperatures is considered to

be outside the pore with a weak interaction between sulfur and carbon material [15]. In accordance with the results, the sulfur in the S/C composites obtained in this work also varies from outside to inside the pore during the infiltration time. A partial amount of sulfur with weak interaction is expected in all the S/C composites including S/C-12 h and S/C-24 h composites in which a slight slope at around 200 °C is observed (Figure 2c). The S/C-1 h composite may have a less interaction of sulfur with carbon material since the sublimation temperature of the sulfur occur at lower temperatures than the other S/C composites. If the sublimation temperature of sulfur occurs at higher temperatures, a stronger interaction between sulfur and carbon material is supposed since this interaction may require more energy to sublime the sulfur in the composite. Thus, the S/C-6 h composite seems to show stronger interaction between sulfur and carbonaceous material than other S/C composites because of the clear shift of the sublimation temperature of sulfur in the S/C-6 h composite observed in Figure 2c. Sulfur infiltration into the MC pores is produced thanks to capillary forces and occurs quickly in the micropores that connect the global structure of the carbonaceous material [38]. Then, the infiltration of the mesopores occurs as the treatment time increases, more sulfur amount incorporation is favored. By having a high proportion of sulfur, at longer infiltration times the total blockage of pores will be promoted. For electrochemical performance perspective, this parameter implies that there is no available space for the lithium ions transport that is incorporated into the material to carry out redox processes; it also does not leave any free space to accommodate the lithium polysulfide species that are formed during the charging/discharging of the cell [39].

Figure 2d–g shows the SEM images of the MC and the S/C composites at different sulfur infiltration times. Figure 2g and Figure S3 (supporting information) shows EDX analysis of S/C composites including carbon and sulfur mapping. The MC particles have a “sausage-like” morphology with micrometer-average size 0.1–0.2 µm characteristic of ordered MC obtained from the SBA-15 template [40,41]. S/C composites maintain the MC morphology; however, a different morphology for S/C-1 h and S/C-24 h composites, forming a kind of a layer, is observed (highlighted with a yellow line). Similar sulfur depositions or agglomerations were verified by EDX analysis indicating that the sulfur is not homogeneously distributed (Figure S3). MC morphology was also confirmed in the S/C-6 h composite with an enhanced distribution of sulfur (Figure 2g). The sulfur distribution in the materials infiltrated at 6 and 24 h was corroborated by transmission electron microscopy (TEM), the result is presented in Figure S4. A better distribution of sulfur can be obtained for the material infiltrated at a shorter time, i.e., S/C 70:30, 6 h. This result is in agreement with that obtained by SEM-EDX indicating that in longer infiltration times not only is a sulfur accumulation on the particle surface but also there is no homogeneous distribution of it within the pores of the mesoporous carbon.

The study of the sulfur infiltration time effect suggests that intermedium times around 6 h are suitable to promote sulfur infiltration or inclusion into the carbonaceous structure with enhanced S-C interaction and sulfur distribution. In the next section, the sulfur content is studied using 6 h for the meting-diffusion process.

2.2. Sulfur Content Effect

Figure 3 shows physicochemical characterization of the S/C composites at different sulfur content. Table 2 summarizes physicochemical properties of these compared with those obtained from MC.

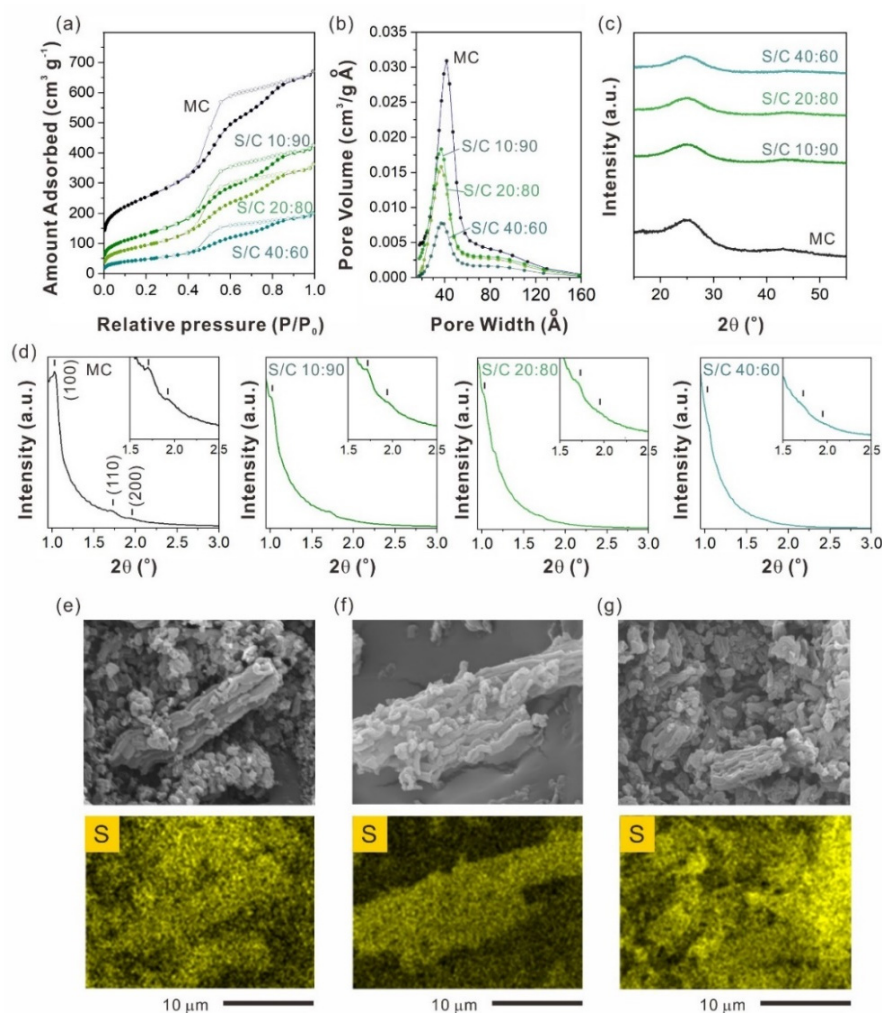


Figure 3. (a) Adsorption and desorption isotherms for MC and S/C composites at different sulfur content. Unfilled symbols correspond to desorption (b) Pore size distribution for MC and S/C composites. (c) XRD patterns of MC and S/C composites at different sulfur content. (d) XRD patterns at small-angle of MC and the S/C composites at different sulfur content. XRD zooming in the inset. Bar indicates (100), (110), and (200) planes. SEM-EDX analysis of S/C composites: (e) S/C–10:90, (f) S/C–20:80 and, (g) S/C–40:60.

Figure 3a,b shows the adsorption/desorption isotherms and pore size distribution for the MC and S/C composites at different sulfur content. The S/C composites profile shows the type IV isotherm, in good agreement with the MC profile (previously described, Figure 2a). Surface area and pore volume of S/C composites monotonically decrease with the sulfur content over 80% (Table 2) suggesting that sulfur is rather infiltrated (pores filling) in the MC microstructure [42]. The pore size distribution of the S/C composites (Figure 3b) matches well with the MC pore distribution keeping the two main pore diameters (Table 2) suggesting that the MC host remains unchanged after sulfur infiltration. Note that this observation cannot be done in the previous section since sulfur in 70 wt.% masked the N_2 adsorption/desorption analysis.

Table 2. Physicochemical properties of the MC and S/C composites at different sulfur content (detailed calculation is explained in Section 3).

Samples	MC	S/C 10:90	S/C 20:80	S/C 40:60
Sulfur content by TGA (%)	-	9.80	21.5	41.0
Specific surface area (m^2/g)	872.8	479.0	352.3	177.6
Pore volume (cm^3/g)	1.04	0.70	0.60	0.40
Lattice crystal parameter, a_0 (\AA)	99.0	100	100	97.0
Pore diameter $D_p,1$ (\AA)	42	38	37	38
Pore diameter $D_p,2$ (\AA)	89	87	87	82
Wall thickness variation, Wt_1 (\AA)	57	63	63	59

Figure 3c displays XRD patterns of MC and S/C composites at different sulfur content. A broad amorphous signal, corresponding to the graphitic form from the carbonaceous material, is observed in the XRD patterns of the S/C composites with a lattice crystal parameter around 100 \AA (Table 2). According to some authors, this indicates that sulfur is highly dispersed inside the pores, instead of being distributed on the MC surface, and also suggests that the formation of large sulfur crystals is suppressed [43,44]. Figure 3d shows the small-angle XRD patterns of the S/C composites. Three characteristic signals at $2\theta < 2^\circ$ corresponding to (100), (110), and (200) planes for the two dimensional (2D) hexagonal p6mm space group of the mesoporous materials are identified [25,45,46]. With the sulfur content increasing in the composites, the (100) peak did not change indicating that the lattice space d100 is conserved. Moreover, the reflection of the planes became weaker as the sulfur amount increased, associated with a change in the wall thickness of the MC host in the S/C composites [14]. The calculated Wt_1 [47] (Table 2) based on the pore diameter centered about 37 \AA slightly increase for the S/C 10:90 and S/C 20:80 composites compared with the MC, indicating that there is an infiltration of this within the pores of the carbonaceous material. This close interaction would improve the sulfur retention inside the pores during cell operation. Wt_1 does not vary significantly when 40 wt.% of sulfur is incorporated, which suggests that part of the sulfur is remaining outside the pores and could be accumulated on the MC surface. Figure 3e–g shows SEM-EDX analysis of the S/C composites at different sulfur content. The materials retain the MC morphology (Figure 2d) as expected. A homogeneous distribution of sulfur is observed for the S/C-10:90 and S/C-20:80 composites (Figure 3e,f) while a saturated signal of sulfur in some regions for the S/C-40:60 composite (Figure 3g) evidences an inhomogeneous distribution of the sulfur.

Figure 4 shows HRTEM images of S/C composites with different sulfur content. The bright contrast strips on the image represent the pore, the composites present an obvious channel pore structure with a regular interval of a linear array of mesopores throughout the samples. This is consistent with the characteristic of the MC employed [48]. The surface of the inner channels (pores) of the carbon seems to be coated, which is due to the sublimed sulfur penetrating the MC channels. The infiltration can be demonstrated by the reduction of the pore width of the MC when the composite is formed with different sulfur contents.

Without sulfur infiltration, the MC presents a pore width centered in 24 \AA , for S/C 10:90 and S/C 20:80 the pore width is centered in 18 \AA and 17 \AA respectively. For S/C 40:60, the pore width is centered at 23 \AA , indicating that the sulfur remained outside the pores and probably, distributing on the MC surface. The pore width behavior of the composites obtained from the HRTEM micrographs agrees with the wall thickness result.

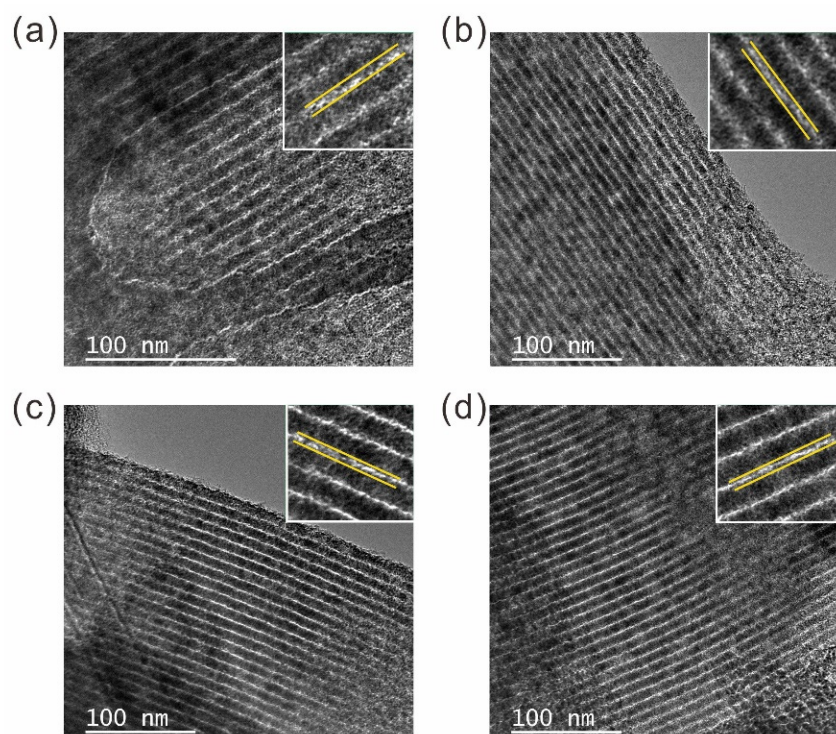


Figure 4. HRTEM images of mesostructured carbon and S/C composites at different sulfur content: (a) MC, (b) S/C 10:90, (c) S/C 20:80, (d) S/C 40:60.

The study of the sulfur content into the MC microstructure suggests that sulfur contents between 10 and 20 wt.% not only allows an effective sulfur infiltration but also an enhanced distribution with an intimate contact between MC host and sulfur. Overall, the preparation of S/C composite by melting-diffusion process allow determining that both facts, sulfur infiltration time and sulfur content, must be controlled to obtain a homogeneous sulfur distribution, a suitable S-C interaction and prevent the large crystallization of sulfur.

2.3. Electrochemical Properties

The S/C composites were evaluated as cathode materials in Li-S cells. The Nyquist plots of the samples are shown in Figure 5a, the semicircles at low frequencies (ca. 10.4, 3.5, and 2.3 Hz for S/C-10:90, S/C-40:60, and S/C-70:30 respectively) are related to the resistance to charge transfer (R_{ct}), that indicates the efficiency of the oxide-reduction processes and electron transfer through the electrode-electrolyte interface [49].

At lower R_{ct} value, the charge/discharge process will be more efficient, and this is related with a good interface contact inside the composite. The S/C-10:90 composite has the lowest R_{ct} value ($35\ \Omega$) indicating fast kinetics. The R_{ct} increases as the sulfur content in the composite is higher due to the insulator nature of the sulfur and can be rather affected by its inhomogeneous distribution into MC microstructure (verified for S/C composites with 40 and 70 wt.% by XRD and SEM-EDX analysis (Figures 2b and 3g)). The Nyquist plots for the samples were fitted using the two equivalent circuits presented in Figure 6. The plots are composed of a small semicircle at high frequencies related to the current collector (R_1), followed by two semicircles caused by the charge transfer of the intermediates produced ($R_2 = R_{ct}$) and by the formation and dissolution of S_8 and Li_2S (R_3), and a straight line representing the diffusion process (Q_D). The diffusion process of soluble polysulfides was fitted with a constant phase element (CPE) instead of a Warburg diffusion element [50,51].

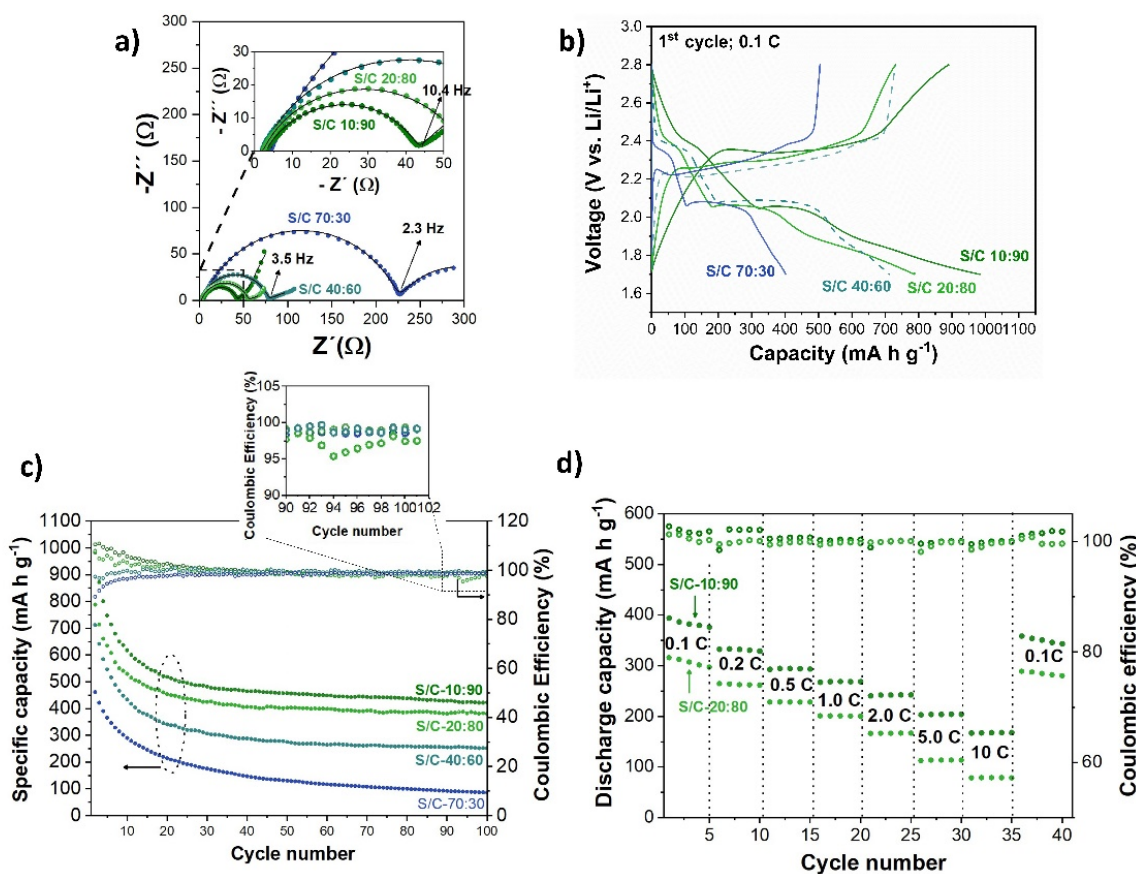


Figure 5. (a) Nyquist plots for the cells before cycling. (b) First charge-discharge curves and (c) cycling performance of the cells using S/C composite electrode at different sulfur content. (d) Rate capabilities of S/C 10:90 and S/C 20:80 composite electrodes.

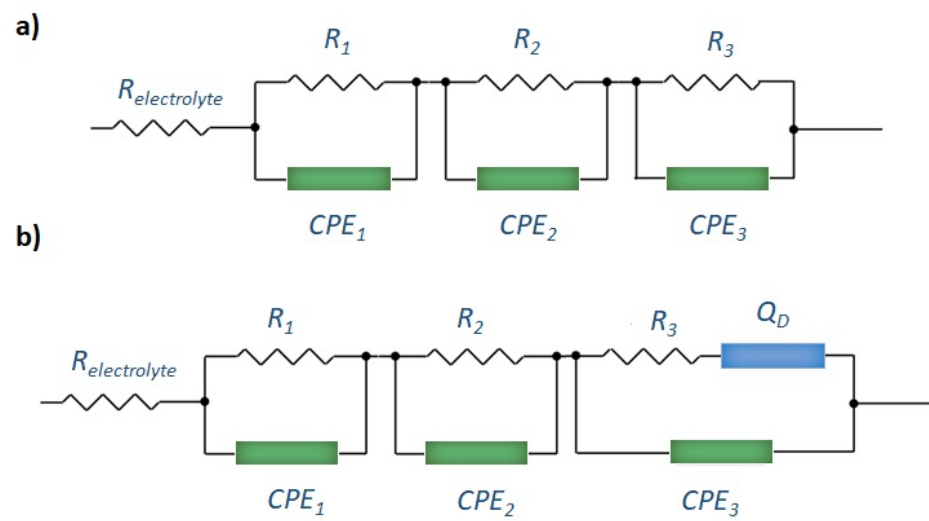


Figure 6. Equivalent circuits for the cells with (a) 70%, and (b) 10–40% of sulfur content.

The cell formed with S/C 70:30 presents a distorted loop at low frequencies, related with a diffusive process through the passivation layer on the lithium surface caused by the sulfur dissolution in the electrolyte that is reduced in the negative electrode [52]. This result is in agreement with the physicochemical characterization where sulfur was found not to be incorporated efficiently in the MC pores, favoring its leaching, and depositing

in the anode, this is also reflected in the resistance related to the electrolyte, which was higher for this cell.

For the straight line, the diffusion coefficient of the ions can be obtained from the equation [53,54]:

$$D = R^2 T^2 / 2 A^2 n^4 F^4 C^2 \sigma^2 \quad (1)$$

Here, D is the diffusion coefficient, R is the gas constant, T is the absolute temperature, A is the surface area, n is the number of electrons, F is the Faraday's constant, C correspond to the ions concentration in the material and σ is the Warburg factor related to Z' obtained from the relationship between Z' and $\omega^{-1/2}$ presented in Figure S5. From Table 3, it can be observed that at higher sulfur content, the diffusion coefficient decreases. The large lithium-ion diffusion coefficient of S/C 10:90 means that the cell formed with this composite possesses a fast ion transfer in the region of the electrolyte/electrode interface. This result is in agreement with the physicochemical and electrochemical results presented in this work; this suggests that sulfur excess also affect the conductivity and mass transfer [55]. The diffusion coefficient for S/C 70:30 was not calculated because the diffusion associated with the straight line at low frequencies was not evident in the impedance spectrum.

Table 3. Impedance parameters of samples and the apparent diffusion coefficients.

Sample	Resistances	Warburg Factor	Diffusivity
	Rs (Ω)	$\Omega s^{-1/2}$	(cm^2/s)
S/C 10:90	2.91	35.0	7.05×10^{-22}
S/C 20:80	2.30	44.4	2.73×10^{-22}
S/C 40:70	2.24	77.1	3.67×10^{-23}
S/C 70:30	4.01	216	—

The charge and discharge capacities of the cells were calculated from the active material mass. The initial discharge profile of the S/C composites shown in Figure 5b exhibits two plateaus at c.a. 2.3 V and 2.1 V, the first plateau corresponding to the transition from S_8 to soluble polysulfides of long chain (Li_2S_8 , Li_2S_6 or Li_2S_4) with fast kinetics, for this reason, this plateau is shorter compared with the second plateau. The reduction of Li_2S_4 to insoluble short chain polysulfides $\text{Li}_2\text{S}_2/\text{Li}_2\text{S}$ is represented by the formation of the second plateau with slow kinetics. The plateau on the charge/discharge profile at the 1st cycle represents the lithium polysulfide species formation due to the cell operation as the voltage changes [56–58].

For the compounds with S/C 10:90 and S/C 20:80, the sulfur content is lower, representing a lower amount of lithium polysulfide species and, therefore, a smaller plateau than S/C 40:60 is observed. When the sulfur content is higher, the plateau of S/C 70:30 should be higher; however, the discharge plateau is smaller than other composite electrodes. The reason for this behavior is associated with the unavailable sulfur for oxidation-reduction processes (verified by SEM analysis, Figure 3e–g) [59]. Although the S/C 40:60 material presents a longer plateau in the first cycle, this behavior is not maintained through the cycling of the cell. Physicochemical results such as small-angle XRD, and sulfur distribution from SEM and TEM images proved that there is higher infiltration efficiency when using low percentages of sulfur that infiltrates into the pores of the carbonaceous material promoting electronic conductivity, and thereby the specific capacity of the cell [60].

Redox conversion reactions of sulfur to polysulfides were also verified in CV curves of the cells [61] (Figure S6a). Firstly, the cell was discharged which means that the sulfur is reduced giving the formation of long-chain lithium polysulfides until reaching short-chain ones ending with the insoluble species Li_2S . Initially, there is the opening of the S_8 ring followed by the formation of long-chain lithium polysulfides (Li_2S_x , $4 \leq x \leq 8$), these reactions are related to the rapid kinetics of the process and are evidenced in the curves with the plateau close to 2.3 V. In a second step, known as slow kinetics, the long-chain lithium polysulfides become short-chain, forming Li_2S_2 and ending up to Li_2S , this

transition of species is related to the reduction plateau that appears at 2.1 V. During cell charging, the short-chain lithium polysulfides are converted back to the long-chain until they reach the initial chemical species. For the composite S/C-10:90, only an oxidation plateau during the charge appears at 2.4 V indicating faster oxidation compared to the other materials [62,63].

The cycling performances presented in Figure 5c for the S/C composites show a higher initial specific discharge capacity for S/C-10:90 (983 mA h g⁻¹). The specific capacities of the cells decrease as the sulfur content increases (788 mA h g⁻¹, 712 mA h g⁻¹, and 401 mA h g⁻¹ for 20 wt.%, 40 wt.%, and 70 wt.% sulfur respectively). This is related to sulfur that cannot be efficiently incorporated into the pores of the MC or with the inhomogeneous distribution on the MC surface; therefore, the sulfur loses physical contact with the conductive carbon particles causing a less access of lithium to sulfur and corresponding conversion reactions. The discharge capacity of Li-S cell using S/C composites suffers a monotonically decrease during the first 20 cycles (Figure S6b) associated with the shuttle reactions and corrosion of lithium anode [8,64]. After 100 cycles the Li-S cell with S/C-10:90 composite shows the highest discharge capacity of 425 mA h g⁻¹ and Coulombic efficiency of 99%. The effect of the sulfur infiltration time (6 and 24 h) was verified in the electrochemical properties of the S/C 10:90 composite (cycling performance at Figure S6c). Basically, S/C 10:90-24 h composite shows a lower capacity compared with the S/C 10:90-6 h which verifies that sulfur infiltration time of 6 h results in a homogeneous sulfur distribution and, therefore, electrochemical performance in Li-S cells.

The E/S (electrolyte/sulfur) ratios for the cathodes with 10, 20, 40, and 70% sulfur are 28.3, 17.4, 8.9, and 5.9 mL g⁻¹, respectively. The increase of E/S ratio usually improves the sulfur utilization and battery kinetics because of control of electrolyte viscosity allows sufficient Li-ion and polysulfide diffusions [65]. Therefore, this fact is also contributing to the enhancement of electrochemical cell of composite electrode with 10%. Note that E/S ratio with values higher than 8–10 mL g⁻¹ shows higher capacity retentions than those reported in this work [66,67], which suggest that the processing of the composite electrode such as infiltration process is critical to achieve high total capacity and capacity retention.

To prove the inclusion effect of nitrogen functionalities in the carbonaceous material, a mesoporous carbon blank without nitrogen content was prepared and infiltrated with 10% of sulfur (undoped S/C 10:90) under the same conditions as infiltration for the material with the best performance (S/C 10:90). Figure S6d shows the evidence of the nitrogen promoting effect, obtaining a higher capacity when nitrogenous groups are present since without doping the capacity obtained was 209.9 mA h g⁻¹. The nitrogen atoms in the network cause the carbon atoms of the pyridine rings to have a partial positive charge. This charge will produce a chemical absorption between the carbonaceous network and the lithium polysulfide anion; therefore, the dissolution of these species is decreased, improving the electrochemical performance of the cell [3,68]. In contrast, for cathodes prepared from mesoporous carbonaceous materials under conventional melting-diffusion conditions (S₈ = 60%, 155 °C, 12 h), an initial capacity of ~800 mA h g⁻¹ at 0.1 C is reported, and after 100 cycles, this capacity decreases up to ~450 mA h g⁻¹ [69], which demonstrates the relevance of the result reported in this work where similar capacity is obtained after 100 cycles but considerably reducing the infiltration time and sulfur content.

Figure 5d shows the rate capability for the samples S/C-10:90 and S/C-20:80, the cells were stabilized at 20 cycles before varying the discharge rate. With 10% sulfur, a higher specific capacity is obtained at the different C-rates. At 0.1 C, the cells show a slight drop in capacity, but it remains constant when the rate is increased. When returning from 10 C to 0.1 C, a recovery of the initial capacity of the cells is observed indicating a reversible and stable behavior. The electrochemical performance of S/C composites in Li-S cells confirms that the well-distributed sulfur in MC structure and intimate contact between them are crucial to achieve higher capacities and a better cyclability.

Further perspectives to enhance the infiltration process includes control of the particle size by grinding mechanisms o solution processes, control of porosity, and the use of

solvents to favor contact between sulfur and the carbonaceous material. Solid electrolytes in Li-S batteries could be also used to achieve superior capacitances [70,71].

3. Materials and Methods

3.1. Preparation of S/C Composites

The nitrogen-doped mesoporous carbon CMK-3 (from here MC) was synthesized using SBA-15 (3.0 g) as a template to replicate its morphology and porosity. 15 mL of ethylenediamine ($\geq 99\%$, Sigma-Aldrich, St. Louis, MO, USA) and 10 mL of carbon tetrachloride (anhydrous $\geq 99.5\%$, Sigma-Aldrich, St. Louis, MO, USA) were employed as nitrogen and carbon source, respectively. The three components were mixed for 12 h seeking to fill the silica porous with the precursors and then heated at 50 °C for 6 h using a reflux system to avoid the reagents evaporation. Afterwards, the impregnated template was dried under vacuum for 12 h and then heat-treated under a nitrogen atmosphere at 850 °C with a rate of 3 °C/min, and an isotherm of 5 h to form the mesoporous carbon material. The template removal was done with HF 10% v/v (48% v/v, Sigma-Aldrich, St. Louis, MO, USA) solution overnight and was then washed several times with deionized water until pH = ~7 and dried at 80 °C. The sulfur infiltration was performed by melting-diffusion process, following a reported procedure [3]. Briefly, MC and sulfur (99.5%, Kanto Chemical, Tokyo, Japan) were macerated for 15 min to form the composite using a 70:30 wt.% ratio (S/C), the mixture was suspended in CS₂ (99.5%, PanReac ApplChem, Darmstadt, Germany) and magnetically stirred for 30 min followed by solvent evaporation. Then, the mixture was pressured and kept at 155 °C variating the time (1, 2, 3, 4, 6, 12, and 24 h) in an autoclave Teflon container. All samples were labeled as S/C-h, with h, indicating the infiltration time. The effect of the sulfur content was evaluated by varying the S:C wt.% ratio (10:90, 20:80, 40:60, 70:30), the samples were labeled as S/C x:y, with x and y indicating sulfur carbon ratio, respectively.

3.2. Characterization

Nitrogen adsorption and desorption isotherms were obtained by using a Brunauer–Emmett–Teller (BET) method. The MC was degassed at 180 °C for 12 h while the S/C composites were treated at 80 °C for 18 h to avoid the sulfur sublimation. The crystalline phase of S/C composites was evaluated by X-ray powder diffraction (XRD) using an X-ray diffractometer (Panalytical, Empyrean Serie 2, Malvern, UK), the diffraction data was collected in 0.01° steps from 15° to 55° in 2θ for wide angle and from 0.8° to 6° in 2θ for small angle using a Co Kα radiation. Phase identification by comparison with ICSD (Inorganic Crystal Structure Database, Bonn, Germany) references. A Thermogravimetric analysis (SDT-Q600 TA Instruments, New Castle, USA) was performed to understand S/C thermal stability from room temperature to 600 °C at 5 °C/min holding during 15 min under nitrogen atmosphere. The morphology and elemental composition analyses of S/C composite were studied through Field Emission Scanning Electron Microscopy (FE-SEM, JEOL JSM-7100F, Tokyo, Japan) coupled with an Oxford energy dispersive spectroscopy (EDX) system. The sulfur distribution in the MC material was studied by transmission electron microscopy (TEM) using a FEI Tecnai F20 Super Twin TEM/STEM (Waltham, USA) scanning transmission electron microscope operated at 200 kV. The preparation of samples for HRTEM analysis involved sonication in ethanol for 2–5 min and deposition on a copper grid. The pore size analysis presented from the high-resolution transmission electron microscopy (HRTEM) results was performed from the use of several micrographs using the ImageJ (Bethesda, USA) tool. The pore measurement was carefully carried out by selecting the areas of the image where there was no problem due to particle thickness or contrast (250 points per sample). The measurements of all the samples presented were taken under the same operating conditions of the equipment maintaining an OL defocus value close to 90% for all cases.

The wall thickness variation (Wt) of MC and MC host in S/C composites was derived by XRD diffraction and nitrogen sorption analyses and calculated according to

$W_t = a_0 - D_p$ [47], where a_0 is the lattice crystal parameter ($a_0 = \frac{2d_{(100)}}{\sqrt{3}}$) and D_p is the pore diameter. The plane distance $d_{(100)}$ can be obtained from the small-angle patterns using the $d_{(100)} = \frac{\lambda}{2\sin\theta}$, $\lambda = 1.54$ Å.

The nitrogen presence in mesoporous carbon and its functionalities were determined by X-ray photoelectron spectroscopy (XPS) and elemental analysis, respectively. The XPS measurement was carried out in a Specs X(NAP-XPS) with PHOIBOS 150 1D-DLD (Berlin, Germany) as analyzer.

3.3. Electrochemical Tests

All the electrochemical tests were carried out in two-electrode cells (flat test cell). The working electrodes were prepared to form a slurry of 70 wt.% S/C composite electrodes, 15 wt.% carbon black super P (TIMCAL, Bironico, Switzerland) as a conductive agent and 15 wt.% polyvinylidene fluoride (PVDF, Sigma-Aldrich, St. Louis, MO, USA) as a binder in 750 μL of N-methyl pyrrolidone (NMP, Merck) as a solvent. The slurry was coated onto a piece of aluminum foil (0.025 × 300 × 300 mm, Nilaco Corp., Tokyo, Japan) using a doctor blade with a thickness of 45 μm and dried overnight at 60 °C. The electrodes were cut into 1 cm circles and dried under vacuum at 60 °C for 6 h before the cell assembly.

1 M lithium bis-(trifluoromethanesulphonyl) imide (LiTFSI, 99.95%, Sigma-Aldrich, St. Louis, MO, USA) dissolved in the mixture of dimethoxymethane (DME, Wako, Tokyo, Japan) and 1,3-dioxolane (DOL, Wako, Tokyo, Japan) (*v/v*, 1:1) was used as the electrolyte; and 0.1 M LiNO₃ (99.99%, Sigma-Aldrich, St. Louis, MO, USA) was dissolved into the electrolyte to help the lithium electrode passivation. All the cells were assembled in an Ar-filled glove box ([O₂] and [H₂O] < 0.5 ppm) using the composite as the working electrode and porous propylene separator (Celgard 2500, MTI Corp., Berkeley, USA), 600 μL of electrolyte and lithium foil (0.025 × 300 × 300 mm, Nilaco, Tokyo, Japan) as the counter electrode. The sulfur loading of the electrodes was 0.28, 0.21, 0.14, and 0.09 mg cm⁻² for the composites with 70, 40, 20, and 10% of sulfur content respectively.

The discharge-charge measurement was initiated with discharge. The cell performance was evaluated in a constant current mode (CC) at room temperature using a charge-discharge device (580 Battery Type System, Scribner Associates, Southern Pines, NC, USA) with C-rates of 0.1, 0.2, 0.5, 1.0, 2.0, 5.0, and 10 C between 1.7 and 2.8 V vs. Li/Li⁺. Electrochemical impedance spectroscopy (EIS) was carried out before cycling cells in the frequency range of 1 MHz to 10 mHz with an amplitude of 10 mV using a Zahner potentiostat (Kronach, Germany). Cyclic voltammetry (CV) was carried out in the range of 1.7 to 2.8 V vs. Li/Li⁺ with a scan rate of 0.1 mV s⁻¹.

4. Conclusions

A series of sulfur-carbon composites were prepared through the melting-diffusion process by modifying the sulfur infiltration time between 1–24 h and the sulfur content. Their structural properties were evaluated and correlated with the electrochemical behavior in Li-S cells.

From the results of nitrogen adsorption isotherms, the cylindric porous microstructure of the carbonaceous material was preserved, and the highest sulfur-mesoporous carbon contact and sulfur homogeneous distribution were obtained with the S/C-10:90 composite infiltrated for 6 h. This was verified by the presence of a broad background (amorphization) of the XRD pattern in the region of $2\theta = 25\text{--}35^\circ$, and the wall thickness obtained for this material showed an increase compared to that of the carbonaceous material without infiltration, which corresponds to efficient infiltration within the pores. In addition, the absence of sulfur-film precipitations was observed from the SEM-EDX analysis, and the HRTEM results showed a decrease in pore size when forming the composite, which indicates that it was possible to incorporate sulfur into the pores of the MC, facilitating the electronic conductivity of the active material.

The Li-S cell using S/C composite formed with 10 wt.% of sulfur at 6 h of infiltration time proves that the sulfur is effectively interacting with the mesoporous carbon resulting

in an initial discharge capacity of 983 mA h g^{-1} , which is significantly higher than S/C composite electrodes infiltrated during longer periods of a time such as 24 h (612 mA h g^{-1}) or higher sulfur content such as 70 wt.% (401 mA h g^{-1}), conditions commonly reported in the literature. After 100 cycles, the discharge capacity obtained was higher than the final capacity of the cell with the other composites corroborating the sulfur infiltration efficiency under these experimental conditions.

Supplementary Materials: The following supporting information can be downloaded at: <https://www.mdpi.com/article/10.3390/batteries8060058/s1>, Figure S1: High-resolution XPS spectra of N1s for MC material; Figure S2: TGA analysis for sulfur sublimation of the S/C composites with 70% of S_8 and modifying the infiltration time; Figure S3: SEM-EDX analysis of (a) S/C-1 h and (b) S/C-24 h. EDX mapping includes carbon and sulfur analysis; Figure S4: TEM elemental mapping of the (a) S/C 70:30, 24 h and (b) S/C 70:30, 6 h composites. Mapping includes sulfur, carbon, and nitrogen analysis; Figure S5: Relationship between Z' and $\omega^{-1/2}$ in the low-frequency region; Figure S6: (a) Cyclic voltammetry (CV) curves of 2nd cycle at scan rate of 0.1 mV s^{-1} (b) Cycling performance efficiency at 0.1 C for 1st and 20th cycle of the cells with the composites variating sulfur content, (c) S/C 10:90 cycling with different infiltration time, and (d) electrochemical comparison of the mesoporous carbon with and without nitrogen functionalization.

Author Contributions: N.C.R.-N., D.L., R.B.-S., A.M. and K.T. conceptualized the idea; N.C.R.-N., D.L. and R.B.-S. also performed supervision of the work; J.L. performed the materials synthesis and characterization and also worked in writing—original draft preparation. N.C.R.-N., D.L., R.B.-S., A.M. and K.T. worked in writing—review and editing. All authors have read and agreed to the published version of the manuscript.

Funding: This research received no external funding.

Institutional Review Board Statement: Not applicable.

Informed Consent Statement: Not applicable.

Data Availability Statement: The data presented in this study are available on request from the corresponding author.

Acknowledgments: The authors wish to thank Universidad de Antioquia UdeA and the Microscopy Laboratory at Instituto Tecnológico Metropolitano (ITM) for their support in the experiments. Jennifer Laverde gratefully acknowledges the Universidad de Antioquia UdeA for her Doctoral scholarship. R.B and D.L wish to thank to Instituto Tecnológico Metropolitano project P20218.

Conflicts of Interest: The authors declare no conflict of interest.

References

- Masoud, E.M. Nano $\alpha\text{-Fe}_2\text{O}_3$ Synthesized Using EDTA-Aqueous Solution Simple and Novel Method: Improved Capacity Retention at 1 C Rate as Anode for High Rate Performance of Lithium-Ion Batteries. *Ionics* **2021**, *27*, 2847–2855. [[CrossRef](#)]
- Zhang, B.; Qin, X.; Li, G.R.; Gao, X.P. Enhancement of Long Stability of Sulfur Cathode by Encapsulating Sulfur into Micropores of Carbon Spheres. *Energy Environ. Sci.* **2010**, *3*, 1531–1537. [[CrossRef](#)]
- Li, X.; Wang, Y.; Xu, C.; Pan, L. Mesoporous Carbon/Sulfur Composite with N-Doping and Tunable Pore Size for High-Performance Li-S Batteries. *J. Solid State Electrochem.* **2017**, *21*, 1101–1109. [[CrossRef](#)]
- Lee, S.; Oh, S.; Park, E.; Scrosati, B.; Hassoun, J.; Park, M.; Kim, Y.; Kim, H.; Belharouak, I.; Sun, Y. Highly Cyclable Lithium-Sulfur Batteries with a Dual-Type Sulfur Cathode and a Lithiated Si/SiO. *Nano Lett.* **2015**, *15*, 2863–2868. [[CrossRef](#)]
- Li, G.; Li, Z.; Zhang, B.; Lin, Z. Developments of Electrolyte Systems for Lithium—Sulfur Batteries: A Review. *Front. Energy Res.* **2015**, *3*, 5. [[CrossRef](#)]
- Liu, Y.; Zhao, X.; Chauhan, G.S.; Ahn, J.H. Nanostructured Nitrogen-Doped Mesoporous Carbon Derived from Polyacrylonitrile for Advanced Lithium Sulfur Batteries. *Appl. Surf. Sci.* **2016**, *380*, 151–158. [[CrossRef](#)]
- Patel, K. Lithium-Sulfur Battery: Chemistry, Challenges, Cost, and Future. *J. Undergrad. Res.* **2016**, *9*, 39–42. [[CrossRef](#)]
- Kumar, R.; Liu, J.; Hwang, J.Y.; Sun, Y.K. Recent Research Trends in Li-S Batteries. *J. Mater. Chem. A* **2018**, *6*, 11582–11605. [[CrossRef](#)]
- Eftekhari, A.; Kim, D.W. Cathode Materials for Lithium-Sulfur Batteries: A Practical Perspective. *J. Mater. Chem. A* **2017**, *5*, 17734–17776. [[CrossRef](#)]
- Dysart, A.D.; Cardoza, N.A.; Mitchell, G.; Ortalan, V.; Pol, V.G. Effect of Synthesis Method Using Varying Types of Micropore Level Sulfur Infiltration on Electrochemical Performance in Lithium–Sulfur Batteries. *Energy Technol.* **2019**, *7*, 1900194. [[CrossRef](#)]

11. Yang, J.Y.; Han, H.J.; Repich, H.; Zhi, R.C.; Qu, C.Z.; Kong, L.; Kaskel, S.; Wang, H.Q.; Xu, F.; Li, H.J. Recent Progress on the Design of Hollow Carbon Spheres to Host Sulfur in Room-Temperature Sodium-Sulfur Batteries. *Xinxing Tan Cailiao/New Carbon Mater.* **2020**, *35*, 630–645. [[CrossRef](#)]
12. Zheng, J.; Gu, M.; Wagner, M.J.; Hays, K.A.; Li, X.; Zuo, P.; Wang, C.; Zhang, J.-G.; Liu, J.; Xiao, J. Revisit Carbon/Sulfur Composite for Li-S Batteries. *J. Electrochem. Soc.* **2013**, *160*, A1624–A1628. [[CrossRef](#)]
13. Li, M.; Carter, R.; Douglas, A.; Oakes, L.; Pint, C.L. Sulfur Vapor-Infiltrated 3D Carbon Nanotube Foam for Binder-Free High Areal Capacity Lithium-Sulfur Battery Composite Cathodes. *ACS Nano* **2017**, *11*, 4877–4884. [[CrossRef](#)] [[PubMed](#)]
14. Jeong, T.G.; Chun, J.; Cho, B.W.; Lee, J.; Kim, Y.T. Enhanced Performance of Sulfur-Infiltrated Bimodal Mesoporous Carbon Foam by Chemical Solution Deposition as Cathode Materials for Lithium Sulfur Batteries. *Sci. Rep.* **2017**, *7*, 42238. [[CrossRef](#)]
15. Suzuki, K.; Tateishi, M.; Nagao, M.; Imade, B.Y.; Yokoi, T.; Hirayama, M.; Tatsumi, T.; Kanno, R. Synthesis, Structure, and Electrochemical Properties of a Sulfur-Carbon Replica Composite Electrode for All-Solid-State Li-Sulfur Batteries. *J. Electrochem. Soc.* **2017**, *164*, A6178–A6183. [[CrossRef](#)]
16. Ji, X.; Lee, K.T.; Nazar, L.F. A Highly Ordered Nanostructured Carbon-Sulphur Cathode for Lithium-Sulphur Batteries. *Nat. Mater.* **2009**, *8*, 500–506. [[CrossRef](#)]
17. Ji, X.; Evers, S.; Black, R.; Nazar, L.F. Stabilizing Lithium-Sulphur Cathodes Using Polysulphide Reservoirs. *Nat. Commun.* **2011**, *2*, 325–327. [[CrossRef](#)]
18. Yan, R.; Oschatz, M.; Wu, F. Towards Stable Lithium-Sulfur Battery Cathodes by Combining Physical and Chemical Confinement of Polysulfides in Core-Shell Structured Nitrogen-Doped Carbons. *Carbon N. Y.* **2020**, *161*, 162–168. [[CrossRef](#)]
19. Abdul Razzaq, A.; Yao, Y.; Shah, R.; Qi, P.; Miao, L.; Chen, M.; Zhao, X.; Peng, Y.; Deng, Z. High-Performance Lithium Sulfur Batteries Enabled by a Synergy between Sulfur and Carbon Nanotubes. *Energy Storage Mater.* **2019**, *16*, 194–202. [[CrossRef](#)]
20. Muthuraj, D.; Ghosh, A.; Kumar, A.; Mitra, S. Nitrogen and Sulfur Doped Carbon Cloth as Current Collector and Polysulfide Immobilizer for Magnesium-Sulfur Batteries. *ChemElectroChem* **2019**, *6*, 684–689. [[CrossRef](#)]
21. Zhao, Y.; Lyu, H.; Liu, Y.; Liu, W.; Tian, Y.; Wang, X. Rational Design and Synthesis of Multimorphology Mesoporous Carbon@silica Nanoparticles with Tailored Structure. *Carbon N. Y.* **2021**, *183*, 912–928. [[CrossRef](#)]
22. Zhao, C.; Liu, L.; Zhao, H.; Krall, A.; Wen, Z.; Chen, J.; Hurley, P.; Jiang, J.; Li, Y. Sulfur-Infiltrated Porous Carbon Microspheres with Controllable Multi-Modal Pore Size Distribution for High Energy Lithium-Sulfur Batteries. *Nanoscale* **2014**, *6*, 882–888. [[CrossRef](#)] [[PubMed](#)]
23. Liu, X.; Zhu, K.; Tian, J.; Tang, Q.; Shan, Z. Preparation of Yolk-Shell Sulfur/Carbon Nanocomposite via an Organic Solvent Route for Lithium-Sulfur Batteries. *J. Solid State Electrochem.* **2014**, *18*, 2077–2085. [[CrossRef](#)]
24. Hossain, M.D.; Zhang, Q.; Cheng, T.; Goddard, W.A.; Luo, Z. Graphitization of Low-Density Amorphous Carbon for Electrocatalysis Electrodes from ReaxFF Reactive Dynamics. *Carbon N. Y.* **2021**, *183*, 940–947. [[CrossRef](#)]
25. Kim, N.I.; Cheon, J.Y.; Kim, J.H.; Seong, J.; Park, J.Y.; Joo, S.H.; Kwon, K. Impact of Framework Structure of Ordered Mesoporous Carbons on the Performance of Supported Pt Catalysts for Oxygen Reduction Reaction. *Carbon N. Y.* **2014**, *72*, 354–364. [[CrossRef](#)]
26. Geng, X.; Rao, M.; Li, X.; Li, W. Highly Dispersed Sulfur in Multi-Walled Carbon Nanotubes for Lithium/Sulfur Battery. *J. Solid State Electrochem.* **2013**, *17*, 987–992. [[CrossRef](#)]
27. Li, K.; Wang, B.; Su, D.; Park, J.; Ahn, H.; Wang, G. Enhance Electrochemical Performance of Lithium Sulfur Battery through a Solution-Based Processing Technique. *J. Power Sources* **2012**, *202*, 389–393. [[CrossRef](#)]
28. Xue, M.; Chen, C.; Tan, Y.; Ren, Z.; Li, B.; Zhang, C. Mangosteen Peel-Derived Porous Carbon: Synthesis and Its Application in the Sulfur Cathode for Lithium Sulfur Battery. *J. Mater. Sci.* **2018**, *53*, 11062–11077. [[CrossRef](#)]
29. He, X.; Hou, H.; Yuan, X.; Huang, L.; Hu, J.; Liu, B.; Xu, J.; Xie, J.; Yang, J.; Liang, S.; et al. Electrocatalytic Activity of Lithium Polysulfides Adsorbed into Porous TiO₂ Coated MWCNTs Hybrid Structure for Lithium-Sulfur Batteries. *Sci. Rep.* **2017**, *7*, 40679. [[CrossRef](#)]
30. Krishnaveni, K.; Subadevi, R.; Radhika, G.; Premkumar, T.; Raja, M.; Liu, W.R.; Sivakumar, M. Carbon Wrapping Effect on Sulfur/Polyacrylonitrile Composite Cathode Materials for Lithium Sulfur Batteries. *J. Nanosci. Nanotechnol.* **2018**, *18*, 121–126. [[CrossRef](#)]
31. Zhao, Y.; Yin, F.; Zhang, Y.; Zhang, C.; Mentbayeva, A.; Umirov, N.; Xie, H.; Bakenov, Z. A Free-Standing Sulfur/Nitrogen-Doped Carbon Nanotube Electrode for High-Performance Lithium/Sulfur Batteries. *Nanoscale Res. Lett.* **2015**, *10*, 450. [[CrossRef](#)] [[PubMed](#)]
32. Ahn, W.; Kim, K.-B.; Jung, K.-N.; Shin, K.-H.; Jin, C.-S. Synthesis and Electrochemical Properties of a Sulfur-Multi Walled Carbon Nanotubes Composite as a Cathode Material for Lithium Sulfur Batteries. *J. Power Sources* **2012**, *202*, 394–399. [[CrossRef](#)]
33. Yang, J.; Xie, J.; Zhou, X.; Zou, Y.; Tang, J.; Wang, S.; Chen, F.; Wang, L. Functionalized N-Doped Porous Carbon Nanofiber Webs for a Lithium-Sulfur Battery with High Capacity and Rate Performance. *J. Phys. Chem. C* **2014**, *118*, 1800–1807. [[CrossRef](#)]
34. Kazazi, M. Synthesis and Elevated Temperature Performance of a Polypyrrole-Sulfur-Multi-Walled Carbon Nanotube Composite Cathode for Lithium Sulfur Batteries. *Ionics* **2016**, *22*, 1103–1112. [[CrossRef](#)]
35. Wang, Y.X.; Huang, L.; Sun, L.C.; Xie, S.Y.; Xu, G.L.; Chen, S.R.; Xu, Y.F.; Li, J.T.; Chou, S.L.; Dou, S.X.; et al. Facile Synthesis of a Interleaved Expanded Graphite-Embedded Sulphur Nanocomposite as Cathode of Li-S Batteries with Excellent Lithium Storage Performance. *J. Mater. Chem.* **2012**, *22*, 4744–4750. [[CrossRef](#)]
36. Hencz, L.; Gu, X.; Zhou, X.; Martens, W.; Zhang, S. Highly Porous Nitrogen-Doped Seaweed Carbon for High-Performance Lithium-Sulfur Batteries. *J. Mater. Sci.* **2017**, *52*, 12336–12347. [[CrossRef](#)]

37. Li, Z.; Yuan, L.; Yi, Z.; Sun, Y.; Liu, Y.; Jiang, Y.; Shen, Y.; Xin, Y.; Zhang, Z.; Huang, Y. Insight into the Electrode Mechanism in Lithium-Sulfur Batteries with Ordered Microporous Carbon Confined Sulfur as the Cathode. *Adv. Energy Mater.* **2014**, *4*, 1301473. [[CrossRef](#)]
38. Xia, Y.; Wang, C.; Li, R.; Fukuto, M.; Vogt, B.D. Sulfur Diffusion within Nitrogen-Doped Ordered Mesoporous Carbons Determined by in Situ X-Ray Scattering. *Langmuir* **2018**, *34*, 8767–8776. [[CrossRef](#)]
39. Bandosz, T.J.; Ren, T.Z. Porous Carbon Modified with Sulfur in Energy Related Applications. *Carbon N. Y.* **2017**, *118*, 561–577. [[CrossRef](#)]
40. Olchowski, R.; Zieba, E.; Giannakoudakis, D.A.; Anastopoulos, I.; Dobrowolski, R.; Barczak, M. Tailoring Surface Chemistry of Sugar-Derived Ordered Mesoporous Carbons towards Efficient Removal of Diclofenac from Aquatic Environments. *Materials* **2020**, *13*, 1625. [[CrossRef](#)]
41. Yu, X.; Nie, R.; Zhang, H.; Lu, X.; Zhou, D.; Xia, Q. Ordered Mesoporous N-Doped Carbon Supported Ru for Selective Adsorption and Hydrogenation of Quinoline. *Microporous Mesoporous Mater.* **2018**, *256*, 10–17. [[CrossRef](#)]
42. Weinberger, C.; Ren, S.; Hartmann, M.; Wagner, T.; Karaman, D.; Rosenholm, J.M.; Tiemann, M. Bimodal Mesoporous CMK-5 Carbon: Selective Pore Filling with Sulfur and SnO₂ for Lithium Battery Electrodes. *ACS Appl. Nano Mater.* **2018**, *1*, 455–462. [[CrossRef](#)]
43. Liu, X.; Rahmatinejad, J.; Ye, Z. Encapsulation of Sulfur within Well-Defined Size-Tunable Ultrasmall Carbon Nanospheres for Superior High-Rate and Long-Stability Li–S Batteries. *Chem. Eng. J.* **2021**, *422*, 130129. [[CrossRef](#)]
44. Luo, C.; Hu, E.; Gaskell, K.J.; Fan, X.; Gao, T.; Cui, C.; Ghose, S.; Yang, X.Q.; Wang, C. A Chemically Stabilized Sulfur Cathode for Lean Electrolyte Lithium Sulfur Batteries. *Proc. Natl. Acad. Sci. USA* **2020**, *117*, 14712–14720. [[CrossRef](#)]
45. Kim, W.; Lee, J.; Lee, S.; Eom, K.S.; Pak, C.; Kim, H.J. Advanced Ordered Mesoporous Carbon with Fast Li-Ion Diffusion for Lithium–Selenium Sulfide Batteries in a Carbonate-Based Electrolyte. *Carbon N. Y.* **2020**, *170*, 236–244. [[CrossRef](#)]
46. Wang, Z.; Li, Y.; Lv, X.J. N-Doped Ordered Mesoporous Carbon as a High Performance Anode Material in Sodium Ion Batteries at Room Temperature. *RSC Adv.* **2014**, *4*, 62673–62677. [[CrossRef](#)]
47. Sanaeishoar, H.; Sabbaghan, M.; Mohave, F. Synthesis and Characterization of Micro-Mesoporous MCM-41 Using Various Ionic Liquids as Co-Templates. *Microporous Mesoporous Mater.* **2015**, *217*, 219–224. [[CrossRef](#)]
48. Vinu, A.; Srinivasu, P.; Sawant, D.P.; Mori, T.; Ariga, K.; Chang, J.S.; Jhung, S.H.; Balasubramanian, V.V.; Hwang, Y.K. Three-Dimensional Cage Type Mesoporous CN-Based Hybrid Material with Very High Surface Area and Pore Volume. *Chem. Mater.* **2007**, *19*, 4367–4372. [[CrossRef](#)]
49. Wei, C.; Han, Y.; Liu, H.; Gan, R.; Li, Q.; Wang, Y.; Hu, P.; Ma, C.; Shi, J. Advanced Lithium–Sulfur Batteries Enabled by a SnS₂-Hollow Carbon Nanofibers Flexible Electrocatalytic Membrane. *Carbon N. Y.* **2021**, *184*, 1–11. [[CrossRef](#)]
50. Cañas, N.A.; Hirose, K.; Pascucci, B.; Wagner, N.; Friedrich, K.A.; Hiesgen, R. Investigations of Lithium-Sulfur Batteries Using Electrochemical Impedance Spectroscopy. *Electrochim. Acta* **2013**, *97*, 42–51. [[CrossRef](#)]
51. Ding, N.; Schnell, J.; Li, X.; Yin, X.; Liu, Z.; Zong, Y. Electrochemical Impedance Spectroscopy Study of Sulfur Reduction Pathways Using a Flexible, Free-Standing and High-Sulfur-Loading Film. *Chem. Eng. J.* **2021**, *412*, 128559. [[CrossRef](#)]
52. Waluś, S.; Barchasz, C.; Bouchet, R.; Alloin, F. Electrochemical Impedance Spectroscopy Study of Lithium–Sulfur Batteries: Useful Technique to Reveal the Li/S Electrochemical Mechanism. *Electrochim. Acta* **2020**, *359*, 136944. [[CrossRef](#)]
53. Zhang, Z.; Chen, D.; Chang, C. Improved Electrochemical Performance of LiNi_{0.8}Co_{0.1}Mn_{0.1}O₂ Cathode Materials: Via Incorporation of Rubidium Cations into the Original Li Sites. *RSC Adv.* **2017**, *7*, 51721–51728. [[CrossRef](#)]
54. Lee, Y.S.; Ryu, K.S. Study of the Lithium Diffusion Properties and High Rate Performance of TiNb₆O₁₇ as an Anode in Lithium Secondary Battery. *Sci. Rep.* **2017**, *7*, 16617. [[CrossRef](#)] [[PubMed](#)]
55. Niu, S.; Lv, W.; Zhang, C.; Li, F.; Tang, L.; He, Y.; Li, B.; Yang, Q.H.; Kang, F. A Carbon Sandwich Electrode with Graphene Filling Coated by N-Doped Porous Carbon Layers for Lithium-Sulfur Batteries. *J. Mater. Chem. A* **2015**, *3*, 20218–20224. [[CrossRef](#)]
56. Cuisinier, M.; Cabelguen, P.E.; Evers, S.; He, G.; Kolbeck, M.; Garsuch, A.; Bolin, T.; Balasubramanian, M.; Nazar, L.F. Sulfur Speciation in Li–S Batteries Determined by Operando X-Ray Absorption Spectroscopy. *J. Phys. Chem. Lett.* **2013**, *4*, 3227–3232. [[CrossRef](#)]
57. Zheng, D.; Liu, D.; Harris, J.B.; Ding, T.; Si, J.; Andrew, S.; Qu, D.; Yang, X.-Q.; Qu, D. Investigation of Li–S Battery Mechanism by Real-Time Monitoring the Changes of Sulfur and Polysulfide Species during the Discharge and Charge. *ACS Appl. Mater. Interfaces* **2017**, *9*, 4326–4332. [[CrossRef](#)]
58. Weng, Y.T.; Wang, H.; Lee, R.C.; Huang, C.Y.; Huang, S.S.; Abdollahifar, M.; Kuo, L.M.; Hwang, B.J.; Kuo, C.L.; Cui, Y.; et al. Efficient Synthesis of High-Sulfur-Content Cathodes for High-Performance Li–S Batteries Based on Solvothermal Polysulfide Chemistry. *J. Power Sources* **2020**, *450*, 227676. [[CrossRef](#)]
59. Wang, N.; Zhang, X.; Ju, Z.; Yu, X.; Wang, Y.; Du, Y.; Bai, Z.; Dou, S.; Yu, G. Thickness-Independent Scalable High-Performance Li–S Batteries with High Areal Sulfur Loading via Electron-Enriched Carbon Framework. *Nat. Commun.* **2021**, *12*, 4519. [[CrossRef](#)]
60. Gueon, D.; Ju, M.-Y.; Moon, J.H. Complete Encapsulation of Sulfur through Interfacial Energy Control of Sulfur Solutions for High-Performance Li–S Batteries. *Proc. Natl. Acad. Sci. USA* **2020**, *117*, 12686–12692. [[CrossRef](#)]
61. Cheng, D.; Wu, P.; Wang, J.; Tang, X.; An, T.; Zhou, H.; Zhang, D.; Fan, T. Synergetic Pore Structure Optimization and Nitrogen Doping of 3D Porous Graphene for High Performance Lithium Sulfur Battery. *Carbon N. Y.* **2019**, *143*, 869–877. [[CrossRef](#)]

62. Huang, H.; Liu, J.; Xia, Y.; Cheng, C.; Liang, C.; Gan, Y.; Zhang, J.; Tao, X.; Zhang, W. Supercritical Fluid Assisted Synthesis of Titanium Carbide Particles Embedded in Mesoporous Carbon for Advanced Li-S Batteries. *J. Alloys Compd.* **2017**, *706*, 227–233. [[CrossRef](#)]
63. Zhang, Y.; Peng, Y.; Wang, Y.; Li, J.; Li, H.; Zeng, J.; Wang, J.; Hwang, B.J.; Zhao, J. High Sulfur-Containing Carbon Polysulfide Polymer as a Novel Cathode Material for Lithium-Sulfur Battery. *Sci. Rep.* **2017**, *7*, 11386. [[CrossRef](#)] [[PubMed](#)]
64. Cao, R.; Xu, W.; Lv, D.; Xiao, J.; Zhang, J.G. Anodes for Rechargeable Lithium-Sulfur Batteries. *Adv. Energy Mater.* **2015**, *5*, 1402273. [[CrossRef](#)]
65. Yan, J.; Liu, X.; Li, B. Capacity Fade Analysis of Sulfur Cathodes in Lithium-Sulfur Batteries. *Adv. Sci.* **2016**, *3*, 1600101. [[CrossRef](#)]
66. Emerce, N.B.; Eroglu, D. Effect of Electrolyte-to-Sulfur Ratio in the Cell on the Li-S Battery Performance. *J. Electrochem. Soc.* **2019**, *166*, A1490–A1500. [[CrossRef](#)]
67. Fan, F.Y.; Chiang, Y.-M. Electrodeposition Kinetics in Li-S Batteries: Effects of Low Electrolyte/Sulfur Ratios and Deposition Surface Composition. *J. Electrochem. Soc.* **2017**, *164*, A917–A922. [[CrossRef](#)]
68. Niu, S.; Zhou, G.; Lv, W.; Shi, H.; Luo, C.; He, Y.; Li, B.; Yang, Q.H.; Kang, F. Sulfur Confined in Nitrogen-Doped Microporous Carbon Used in a Carbonate-Based Electrolyte for Long-Life, Safe Lithium-Sulfur Batteries. *Carbon N. Y.* **2016**, *109*, 1–6. [[CrossRef](#)]
69. Cheng, R.; Guan, Y.; Luo, Y.; Zhang, C.; Xia, Y.; Wei, S.; Zhao, M.; Lin, Q.; Li, H.; Zheng, S.; et al. Guanine-Assisted N-Doped Ordered Mesoporous Carbons as Efficient Capacity Decaying Suppression Materials for Lithium-Sulfur Batteries. *J. Mater. Sci. Technol.* **2022**, *101*, 155–164. [[CrossRef](#)]
70. Pan, H.; Cheng, Z.; He, P.; Zhou, H. A Review of Solid-State Lithium-Sulfur Battery: Ion Transport and Polysulfide Chemistry. *Energy Fuels* **2020**, *34*, 11942–11961. [[CrossRef](#)]
71. Kang, N.; Lin, Y.; Yang, L.; Lu, D.; Xiao, J.; Qi, Y.; Cai, M. Cathode Porosity Is a Missing Key Parameter to Optimize Lithium-Sulfur Battery Energy Density. *Nat. Commun.* **2019**, *10*, 4597. [[CrossRef](#)] [[PubMed](#)]